

# Impact of Lithium Nonstoichiometry on Ionic Diffusion in Tetragonal Garnet-Type $\text{Li}_7\text{La}_3\text{Zr}_2\text{O}_{12}$

Zihan Yan and Yizhou Zhu\*



Cite This: <https://doi.org/10.1021/acs.chemmater.4c02454>



Read Online

ACCESS |



Metrics & More

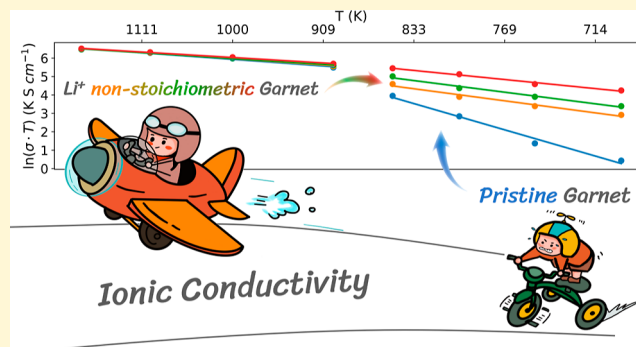


Article Recommendations



Supporting Information

**ABSTRACT:** Understanding ion transport mechanisms on the atomistic scale in solid-state electrolytes is crucial for the development of all-solid-state batteries.  $\text{Li}_7\text{La}_3\text{Zr}_2\text{O}_{12}$  (LLZO) is a promising oxide solid electrolyte material, whose phase transition behavior and ion transport mechanisms have attracted significant research attention. Previous studies have primarily focused on ion transport in the cubic phase (intrinsic high-temperature phase or doped variants). In contrast, the tetragonal phase of LLZO, despite its close relationship with the cubic phase, has received less attention due to its relatively low ionic conductivity and high computational cost. A few recent computational studies have shown significant discrepancies in conductivity and activation energy between calculated and experimental values. Therefore, the unclear ion transport mechanisms in the tetragonal phase of LLZO are critical to understanding and designing oxide solid electrolytes. In this study, we employ state-of-the-art machine-learning-based neuroevolution potential molecular dynamics simulations to investigate the effects of lithium nonstoichiometry on the ionic conductivity and phase stability of LLZO. We demonstrate that small deviations from stoichiometry, particularly lithium deficiency, dramatically reduce the activation energy for  $\text{Li}^+$  diffusion in tetragonal LLZO from 1.227 to 0.425 eV, increasing room-temperature ionic conductivity by 10 orders of magnitude. The slight lithium nonstoichiometry, which commonly occurs during high-temperature synthesis, has a significant effect on ion transport in the tetragonal phase. Our findings highlight the crucial role of lithium nonstoichiometry and defect chemistry in enhancing LLZO performance and provide insights for the rational design of high-performance solid electrolytes through defect engineering.



## INTRODUCTION

All-solid-state lithium-ion batteries have attracted much attention due to their potential to overcome the safety issues and energy density limitations of conventional liquid electrolyte batteries.<sup>1</sup> Among various solid electrolyte materials, garnet-type  $\text{Li}_7\text{La}_3\text{Zr}_2\text{O}_{12}$  (LLZO) is a promising candidate due to its high ionic conductivity,<sup>2–4</sup> negligible electronic transport,<sup>3</sup> wide electrochemical window,<sup>5,6</sup> and stability against Li metal anodes.<sup>6,7</sup> These properties make LLZO a highly promising candidate for next-generation lithium-ion batteries, which has the potential to drive significant advances in high-energy-density electric vehicles, portable electronics, grid energy storage devices, etc.<sup>4,8</sup> LLZO has two different structural phases: a high-temperature cubic phase and a low-temperature tetragonal phase, with ionic conductivity that differs by 2 orders of magnitude.<sup>9</sup> The cubic LLZO (*c*-LLZO), stable above the critical temperature ( $T_c$ ) of  $\sim 900$  K,<sup>9,10</sup> features a disordered Li sublattice that facilitates rapid  $\text{Li}^+$  ion movement, resulting in superior ionic conductivity.<sup>11</sup> In contrast, the tetragonal LLZO (*t*-LLZO) is stable at room temperature but has a fully ordered Li sublattice, which significantly increases the  $\text{Li}^+$  ion diffusion barrier and reduces

its ionic conductivity. Despite that both phases share similar frameworks and closely related ion diffusion mechanisms, the ion diffusion rate in *t*-LLZO at room temperature is 2 orders of magnitude lower than that in *c*-LLZO, and its ion diffusion behavior at the atomic scale is largely overlooked and rarely explored. *c*-LLZO has attracted significant experimental and theoretical interest due to its high ionic conductivity.<sup>12–14</sup> For example, Geiger et al. studied the stability and the correlation between crystal chemistry and ionic conduction in *c*-LLZO. Jalem et al. successfully employed ab initio molecular dynamics (AIMD) simulations to investigate the  $\text{Li}^+$  diffusion mechanism in *c*-LLZO.<sup>14</sup> However, despite these advancements in understanding *c*-LLZO, theoretical studies have struggled to reconcile predictions with experimental observations in *t*-

Received: September 1, 2024

Revised: November 10, 2024

Accepted: November 12, 2024

LLZO, particularly concerning the activation energy for  $\text{Li}^+$  ion diffusion. The experimentally measured activation energy of *t*-LLZO is around 0.45 eV.<sup>15</sup> Such a high activation energy makes it nearly impossible to conduct long-term simulations using computationally expensive methods like AIMD. To overcome this challenge, Lai and Klenk attempted to study the  $\text{Li}^+$  diffusion mechanism in *t*-LLZO using classical molecular dynamics simulations based on Buckingham potentials.<sup>16</sup> However, their follow-up work revealed the presence of significant finite-size effects in *t*-LLZO.<sup>17</sup> They found that a  $1 \times 1 \times 1$  cell simulation produced markedly different results compared to larger supercells, with larger systems yielding higher activation energies. This finite-size effect casts doubt on the reliability of small-scale simulations, underscoring the need for larger computational models. Thanks to the recent development of machine learning force fields, high-accuracy and low-cost large-scale molecular dynamics simulations now allow for direct investigation of the  $\text{Li}^+$  ion transport mechanism in solid electrolytes.<sup>18–20</sup> After, Lai et al. employed a machine learning interatomic potential to simulate a larger  $2 \times 2 \times 2$  supercell of *t*-LLZO, obtaining an activation energy of 1.33 eV.<sup>18</sup> This result is significantly higher than the experimentally observed 0.45 eV.<sup>15</sup> This discrepancy underscores the need for a more comprehensive understanding of the ion diffusion mechanism in *t*-LLZO.

Recent studies have highlighted the crucial role of composition in determining the properties of LLZO.<sup>21,22</sup> For example, an experimental study by Kubicek et al. revealed oxygen nonstoichiometry in LLZO, which inherently leads to lithium nonstoichiometry due to charge balance requirements and significantly affects its overall defect chemistry.<sup>21</sup> Lithium evaporation could occur under elevated temperatures during synthesis, which could lead to either nonstoichiometry in the target garnet phase or the formation of impurity phases. Therefore, using an excess amount of lithium in the starting materials has become a common practice in garnet synthesis. Paoletta et al. found that the lithium nonstoichiometry resulting from lithium loss could have a profound impact on phase stability and ionic diffusion properties.<sup>22</sup> However, how lithium nonstoichiometry affects the structure and  $\text{Li}^+$  ions transport properties in *t*-LLZO remains unclear.

In this study, we employ state-of-the-art machine learning molecular dynamics (MLMD) simulations to investigate the  $\text{Li}^+$  ion transport mechanism in *t*-LLZO. We reveal that nonstoichiometry, resulting from lithium loss commonly observed during high-temperature sintering in solid-state synthesis,<sup>22</sup> strongly dictates the  $\text{Li}^+$  ion diffusion behavior in *t*-LLZO. Remarkably, a small deviation from lithium stoichiometry (0.4%–1.8%) dramatically reduces the activation energy for  $\text{Li}^+$  ion diffusion in *t*-LLZO from 1.227 to 0.425 eV, increasing room-temperature ionic conductivity by 10 orders of magnitude. Our work resolves the longstanding discrepancy between computational predictions and experimental measurements, providing a more realistic physical model of *t*-LLZO. In addition, we found that, as the lithium deficiency concentration increases to about ~3.6%, these vacancies start to affect the phase transition behavior and reduce the  $T_c$  of the tetragonal-to-cubic phase transition, thereby stabilizing high-conductivity *c*-LLZO at lower temperatures. Our work not only contributes to the fundamental understanding of defect chemistry in garnet-type LLZO but also offers practical guidance for optimizing LLZO performance through controlled lithium nonstoichiometry, potentially

accelerating the development of all-solid-state lithium-ion batteries.

## MATERIALS AND METHODS

**LLZO Structures.** The structure of LLZO is characterized by a framework of  $\text{LaO}_8$  polyhedra and  $\text{ZrO}_6$  octahedra, which form a three-dimensional network that hosts  $\text{Li}^+$  ions. Figure 1 illustrates the

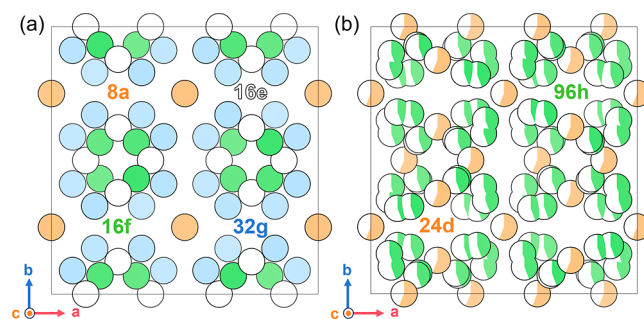


**Figure 1.** Li sublattice in the (a) tetragonal and (b) cubic phases of LLZO.

$\text{Li}^+$  ion sublattices in both *t*-LLZO and *c*-LLZO. In *t*-LLZO (Figure 1a),  $\text{Li}^+$  ions occupy well-defined crystallographic sites, including tetrahedral (8a) and octahedral (16f and 32g) positions. Additionally, there are unoccupied interstitial sites (16e). Such a fully ordered lithium sublattice hinders the fast lithium ion diffusion in *t*-LLZO, resulting in high activation energy for  $\text{Li}^+$  ion hopping. Consequently,  $\text{Li}^+$  ions primarily undergo local vibrations and struggle to achieve long-range migrations, which explains the low ionic conductivity of *t*-LLZO. In contrast, the cubic phase (Figure 1b) exhibits a more disordered  $\text{Li}^+$  ion distribution. Here,  $\text{Li}^+$  ions partially occupy tetrahedral (24d) and octahedral (96h) sites. These partial occupancies feature a disordered  $\text{Li}^+$  ion sublattice, contributing to the higher ionic conductivity observed in *c*-LLZO.

**Density Functional Theory (DFT) Calculations.** All the calculations were performed using the Vienna Ab initio Simulation Package (VASP),<sup>23,24</sup> based on DFT<sup>25,26</sup> within the projector-augmented wave method.<sup>27</sup> The exchange–correlation energy was described by the generalized gradient approximation with the revised Perdew–Burke–Ernzerhof for solids (PBEsol) exchange functional.<sup>28,29</sup> The energy cutoff of the plane wave basis was set to 520 eV. The convergence accuracy for energy was  $1 \times 10^{-4}$  eV within the calculations. The gamma-centered *k*-point meshes with a density of  $0.28 \text{ \AA}^{-1}$  in the Brillouin zone were used for the electronic self-consistent calculation. pymatgen,<sup>30</sup> VASPkit,<sup>31</sup> and VESTA<sup>32</sup> were used for data processing and graphics production.

**Generation of Training Structures.** The initial training set comprised 630 structures of LLZO collected through random perturbations, strains, and the active learning strategy of the moment tensor potential.<sup>33,34</sup> Subsequently, DeepMD-kit<sup>35,36</sup> and DPGEN<sup>37</sup> were employed for automated phase space explorations. We conducted a total of 16 iterations of phase space exploration within the temperature range of 100–1300 K. Details regarding DPGEN can be found in the Supporting Information (Table S1). In addition, we used neuroevolution potential (NEP)<sup>38–41</sup> to sample five random structures with an oxygen and two lithium defects for 1 ns and used farthest point sampling implemented in pynept to select the defect structures for calibrating the energy of LLZO with vacancies. Finally, our training data set of 2024 structures consisted of 1978 pristine LLZO structures and 46 LLZO structures with Li–O defects. Additionally, we sampled 1 ns for LLZO supercell structures of  $1 \times 1 \times 2$ ,  $2 \times 1 \times 1$ , and  $2 \times 2 \times 1$ , each containing one oxygen and two lithium defects, and selected 20 representative structures from each supercell for validation (Figure S2 in the Supporting Information). After evaluating the performance of moment tensor potential, deep potential,<sup>35,42</sup> and NEP, we ultimately selected the NEP model due to

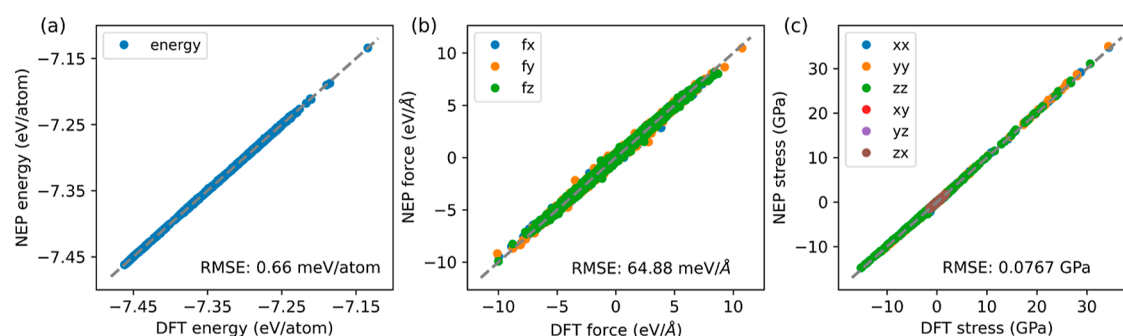


**Figure 2.** (a) Energy, (b) force, and (c) stress values from the NEP model, in comparison to the DFT reference data.

its excellent balance between simulation accuracy and computational speed (see the comparison of moment tensor potential, deep potential, and NEP in the Supporting Information).

**Neuroevolution Potential.** We employed the fourth generation of the NEP model<sup>41</sup> proposed by Fan et al. to construct our interatomic potential for LLZO. The training hyperparameters are listed in the Supporting Information (Table S2). A cutoff radius of 7.5 and 4 Å was adopted for the radial and angular components, respectively. The expansion order for three-body and four-body angular terms was  $l_{\max}^{3b} = 4$  and  $l_{\max}^{4b} = 2$ . We performed  $2 \times 10^5$  iterations to obtain a converged NEP4 model. The root-mean-square errors of energies, forces, and stresses for the training set were 0.66 meV/atom, 64.88 meV/Å, and 0.0767 GPa, respectively (Figure 2).

**Molecular Dynamics Simulation.** MLMD simulations were performed using Graphics Processing Units Molecular Dynamics.<sup>40</sup> We performed 200 ps MLMD simulations to obtain the equilibrium lattice parameters of a  $4 \times 4 \times 4$  supercell of LLZO with or without vacancies at different temperatures by using Martyna–Tuckerman–Tobias–Klein integrators to perform simulations in the isothermal–isobaric (NPT) ensembles with the timesteps of 1 fs. MLMD simulations for ion diffusion were performed in a  $2 \times 2 \times 2$  supercell with the same integrators and ensembles for 2 ns. The diffusivity of  $\text{Li}^+$  ions was calculated as the mean square displacement over time intervals as in previous works<sup>43</sup>

$$D = \frac{1}{2Nd\Delta t} \sum_{i=1}^N \langle |r_i(t + \Delta t) - r_i(t)|^2 \rangle_t \quad (1)$$

where  $N$  is the total number of diffusion ions,  $d = 3$  denotes the dimension of the diffusion system,  $r_i(t)$  is the displacement of the  $i$ -th ion at time  $t$ , and the bracket represents averaging over  $t$ . The ionic conductivity ( $\sigma$ ) is then determined using the Nernst–Einstein relation

$$\sigma = \frac{nq^2}{k_B T} D \quad (2)$$

where  $n$  is the number of mobile ions per unit volume,  $q$  is the ionic charge,  $k_B$  is the Boltzmann constant, and  $T$  is the temperature.

## RESULTS AND DISCUSSION

We first validate our machine learning interatomic potential in terms of the lattice parameters and thermal expansion behaviors. The thermal expansion behavior of LLZO in the temperature range of 100–1300 K was studied by MLMD simulations. Figure 3 illustrates the change in lattice parameters with temperature. Below the  $T_c$  of  $\sim 900$  K, the lattice remains tetragonal ( $a = b > c$ ) with  $a$  and  $c$  exhibiting linear thermal expansion but at different rates, resulting in a gradual decrease of the  $a/c$  ratio with increasing temperature (Figure S1 in the Supporting Information). This anisotropic thermal expansion reflects the inherent structural anisotropy of the tetragonal phase. At the  $T_c$  of  $\sim 900$  K, the lattice

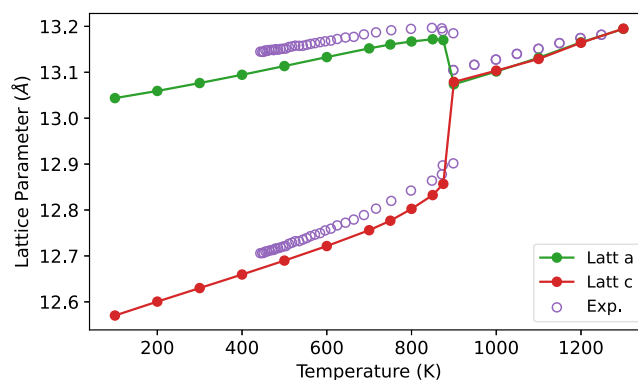


**Figure 3.** Evolution of the calculated lattice parameters of LLZO with simulation temperatures at 100–1300 K. The purple hollow circles represent the experimental lattice parameters from ref 10.

parameters change significantly.  $a$  and  $b$  suddenly decrease, while  $c$  increases, resulting in a cubic unit cell ( $a = b = c$ ). This abrupt change in lattice parameters indicates a phase transition from  $t$ -LLZO to  $c$ -LLZO, and it is accompanied by an order–disorder transition of the lithium sublattice. The calculated lattice parameters exhibit excellent agreement with experimental data (purple hollow circles) from Chen et al.,<sup>10</sup> verifying the accuracy of our NEP model for the description of various properties of both phases of LLZO, such as lattice parameters, phase transition behaviors, and thermal expansion coefficients.

LLZO is a typical ionic compound, in which dominating defects are likely to be charge-compensating ion defect pairs. Previous first-principles calculations confirmed that the Li–O Schottky pair has the lowest formation energy,<sup>44</sup> consistent with the commonly observed lithium loss in synthesis. Additionally, Kubicek et al. reported oxygen nonstoichiometry of approximately  $5 \times 10^{-3}$  per unit cell in LLZO single crystals.<sup>21</sup> Hence, we considered a series of compositions  $\text{Li}_{7-2x}\text{La}_3\text{Zr}_2\text{O}_{12-x}$  ( $x = 0-0.125$ ), corresponding to different degrees of nonstoichiometry. We used MLMD to study the impact of such nonstoichiometry on the ionic conductivity of LLZO.

We found that in stoichiometric  $t$ -LLZO, the calculated activation energy exhibits a large discrepancy from experimentally measured values. Figure 4 presents the Arrhenius plot of  $\text{Li}^+$  ion diffusion in LLZO systems. In pristine  $t$ -LLZO without defects, our MLMD simulations predict a remarkably high activation energy (1.227 eV) for  $\text{Li}^+$  ion diffusion. This predicted value is significantly higher than the experimental value of about 0.45 eV.<sup>15</sup> According to our simulation results, the  $\text{Li}^+$  ions' mobility in defect-free  $t$ -LLZO is severely limited



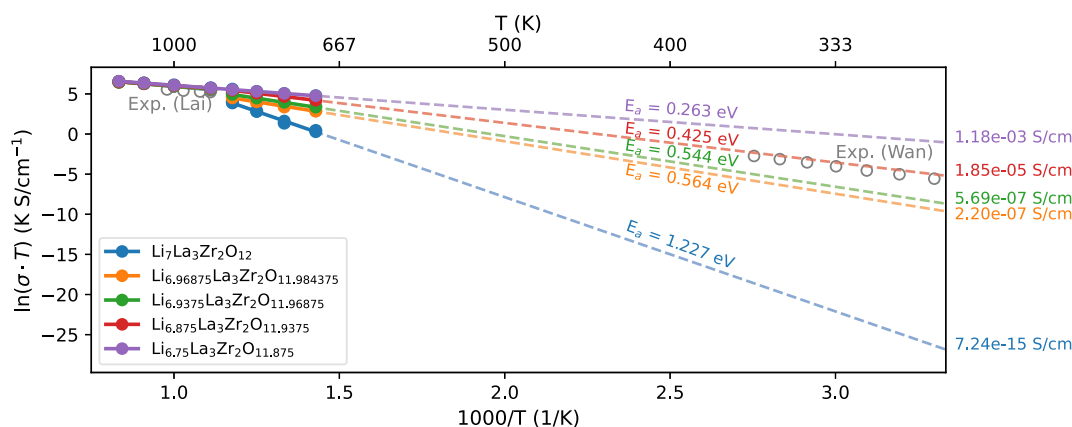


**Figure 4.** Arrhenius plot of  $\text{Li}^+$  ion diffusion in tetragonal and cubic LLZO within different lithium nonstoichiometries. The gray hollow circles represent the experimental results obtained from refs 9 and 15.

and it is impossible to achieve an ionic conductivity of  $\sim 10^{-5}$  to  $10^{-6}$   $\text{S cm}^{-1}$  at room temperature. These large deviations seem to indicate that the simulations give a completely wrong prediction. Nevertheless, this extremely high activation energy we calculated is consistent with the previous theoretical study (1.33 eV) by Lai et al. using the SIMPLE-NN package.<sup>18</sup> Since the two studies adopted different machine learning potential architectures and training data set sampling approaches, this large discrepancy in activation energy between computation and experiments is less likely to result from inaccuracies in the machine learning force field or an improper training process. Instead, it is more likely due to atomistic-scale diffusion mechanisms.

Lithium nonstoichiometry, however, dramatically alters the lithium diffusion behaviors in *t*-LLZO. The introduction of partial Schottky defects ( $2V_{\text{Li}}' + V_{\text{O}}^{\bullet\bullet}$ ) leads to a substantial reduction in the activation energy (Table 1). For the lowest

**Table 1.** Activation Energies of Lithium Ion Diffusion in Tetragonal and Cubic LLZO with Different Degrees of Nonstoichiometry<sup>a</sup>

model	$x$	$E_a$ ( <i>t</i> -LLZO)	$E_a$ ( <i>c</i> -LLZO)
$\text{Li}_7\text{La}_3\text{Zr}_2\text{O}_{12}$	0	1.227	0.309
$\text{Li}_{6.96875}\text{La}_3\text{Zr}_2\text{O}_{11.984375}$	1/64	0.564	0.290
$\text{Li}_{6.9375}\text{La}_3\text{Zr}_2\text{O}_{11.96875}$	1/32	0.544	0.272
$\text{Li}_{6.875}\text{La}_3\text{Zr}_2\text{O}_{11.9375}$	1/16	0.425	0.256
$\text{Li}_{6.75}\text{La}_3\text{Zr}_2\text{O}_{11.875}$	1/8		0.263
exp. (Lai)		0.410	0.210
exp. (Wan)		0.450	

<sup>a</sup>Varying concentrations of partial Schottky defect pairs ( $2V_{\text{Li}}' + V_{\text{O}}^{\bullet\bullet}$ ) were considered in a series of composition  $\text{Li}_{7-2x}\text{La}_3\text{Zr}_2\text{O}_{12-x}$  ( $x = 0-0.125$ ). The experimental results were obtained from refs 9 and 15.

concentration,  $x = 0.016$  we explored, the activation decreases to 0.564 eV, and it continues to decrease as  $x$  increases. This trend indicates that the Schottky defects play a key role in the ion diffusion of *t*-LLZO. Notably, our simulation results are in good agreement with the experimental data reported by Wan et al.<sup>15</sup> when the oxygen vacancy concentration is  $\sim 0.52\%$  (for  $\text{Li}_{6.875}\text{La}_3\text{Zr}_2\text{O}_{11.9375}$ , there are 4 oxygen vacancies in a  $2 \times 2 \times 2$  supercell of LLZO, with a total of 768 oxygen atoms). This concentration is in striking agreement with experimental estimations, as Kubicek et al. reported that “For the highest values measured on the single crystal, this would mean an

oxygen nonstoichiometry of  $\sim 5 \times 10^{-3}$  per unit cell as a first rough estimate”.<sup>21</sup> Interestingly, when we further increase the nonstoichiometry  $x$  to 0.125,  $\text{Li}_{6.75}\text{La}_3\text{Zr}_2\text{O}_{11.875}$ , the activation energy plummets to 0.263 eV, which is very close to a typical Ta-doped *c*-LLZO with a lithium stoichiometry of 6.75.<sup>45</sup> This induced change in  $T_c$  is consistent with the conventional doping strategy used to stabilize the cubic phase, where the nonstoichiometry of lithium is the key to stabilizing the cubic phase (Figure 6).

Compared to that in *t*-LLZO, the activation energy in *c*-LLZO remains around 0.256–0.309 eV (Table 1), with insensitivity to changes in Li–O Schottky defect concentration. This can be attributed to the partially occupied Li sites in *c*-LLZO, which makes it less susceptible to additional  $\text{Li}^+$  vacancies. Besides, the predictions of the ionic conductivity and activation energy of *c*-LLZO by our NEP model are also in good agreement with the experimental results of Lai and Wang (Figure 4).<sup>9</sup>

To elucidate the specific contributions of lithium and/or oxygen nonstoichiometry to the reduced activation energies and enhanced ionic conductivity in *t*-LLZO, we constructed another two models, where only lithium vacancies or oxygen vacancies are present (without charge neutrality). Figure 5 reveals a clear demarcation in both activation energies and ionic conductivities between the lithium and oxygen nonstoichiometric LLZO. Specifically, the experimental result and both  $\text{Li}_{6.875}$  systems (with and without oxygen vacancies) exhibit markedly lower activation energies (0.334–0.450 eV) and correspondingly higher ionic conductivities ( $10^{-5}$  to  $10^{-4}$   $\text{S cm}^{-1}$ ) at 300 K. In contrast, the system with only oxygen nonstoichiometry and the pristine *t*-LLZO demonstrate substantially higher activation energies (1.154 and 1.227 eV) and consequently lower ionic conductivities ( $10^{-15}$  to  $10^{-13}$   $\text{S cm}^{-1}$ ). This disparity unequivocally indicates that lithium nonstoichiometry is the primary driving factor behind the reduced activation energy and enhanced ionic conductivity in *t*-LLZO, while oxygen nonstoichiometry is mainly responsible for maintaining charge neutrality with lithium nonstoichiometry.

In addition to this, lithium nonstoichiometry can also reduce the  $T_c$  of the phase transition of LLZO. Figure 6 illustrates the evolution of LLZO lattice parameters for the pristine and lithium and/or oxygen nonstoichiometry LLZO in the temperature range of 600–1100 K. With the introduction of lithium nonstoichiometry, we observe an expansion along the

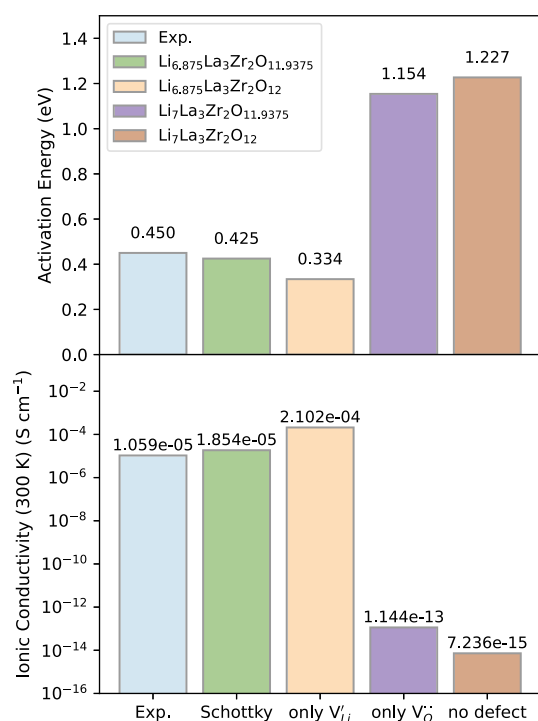


**Figure 5.** Activation energy and ionic conductivity of Li<sup>+</sup> ions in tetragonal LLZO with different types of defects. The experimental results were obtained from ref 15.

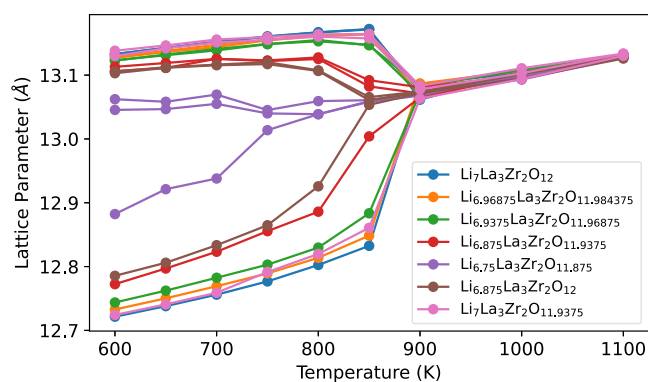


**Figure 6.** Evolution of the lattice parameters for the pristine and lithium and/or oxygen nonstoichiometry LLZO, simulated temperatures ranging from 600 to 1100 K. For each composition, the three lines with the same color and marker represent the *a*, *b*, and *c* lattice parameters, respectively. The lattice parameter values are provided in Table S3.

*c*-axis, while the *a*- and *b*-axes shrink slightly. At an oxygen defect concentration of  $\sim 5.2\%$  ( $\text{Li}_{6.875}\text{La}_3\text{Zr}_2\text{O}_{11.9375}$ ), a significant change in the *a/c* ratio is observed in the temperature range of 750–900 K (Figure S1 in the Supporting Information). Consistent with the results in Figure 5, we notice that this lattice change mainly comes from lithium nonstoichiometry rather than oxygen, as confirmed by the comparison among  $\text{Li}_{6.875}\text{La}_3\text{Zr}_2\text{O}_{11.9375}$ ,  $\text{Li}_{6.875}\text{La}_3\text{Zr}_2\text{O}_{12}$ , and  $\text{Li}_7\text{La}_3\text{Zr}_2\text{O}_{11.9375}$ . Only oxygen nonstoichiometry without lithium nonstoichiometry will still maintain the lattice of pristine LLZO, but the lattice changes significantly when lithium nonstoichiometry is introduced. Besides, in the system of  $\text{Li}_{6.75}\text{La}_3\text{Zr}_2\text{O}_{11.875}$ , we notice a significant decrease in the  $T_c$  of this phase transition from 900 K to about 750 K, which

proves that lithium nonstoichiometry plays a crucial role in regulating the phase stability of LLZO.

## CONCLUSIONS

Our study reveals the impact of lithium nonstoichiometry on the ionic conductivity and phase transition of LLZO. Through MLMD simulations, we demonstrate that even small deviations from stoichiometry can dramatically enhance ionic conductivity in tetragonal LLZO by reducing the activation energy for Li<sup>+</sup> ion diffusion. The stoichiometric *t*-LLZO is predicted to have an extremely high activation energy of 1.227 eV. In contrast, by introducing slight nonstoichiometry with partial Li–O Schottky defects to  $\text{Li}_{7-2x}\text{La}_3\text{Zr}_2\text{O}_{12-x}$  ( $x = 0.0625$ ), the activation energy decrease to 0.425 eV, closely matching experimental observations and increasing room-temperature ionic conductivity by 10 orders of magnitude. Our analysis reveals that lithium-ion diffusion in *t*-LLZO is mainly driven by lithium vacancies rather than oxygen vacancies. Therefore, ion diffusion in stoichiometric *t*-LLZO is limited due to the lack of carriers. Schottky-type defects, which are likely to occur during high-temperature synthesis, lead to an increase of carrier concentrations and an increase of ionic conductivity. Moreover, we found that increasing lithium nonstoichiometry can lower the  $T_c$  for the tetragonal-to-cubic phase transition, potentially stabilizing the highly conductive cubic phase at lower temperatures. This trend is in line with the traditional doping strategy to stabilize the cubic phase.

These findings provide crucial insights into the atomic-scale mechanisms underlying the enhanced performance of non-stoichiometric LLZO and offer a promising avenue for the optimization of solid electrolytes through defect engineering. Our work bridges the gap between theoretical predictions and experimental observations, emphasizing the necessity of incorporating realistic defect concentrations in theoretical studies. In addition, this study underscores the critical importance of considering and controlling the lithium content in the development of high-performance all-solid-state lithium batteries. It opens new avenues for tailoring the properties of solid electrolytes through careful manipulation of stoichiometry, paving the way for the rational design of next-generation solid electrolytes with enhanced ionic conductivity and improved phase stability.

## ASSOCIATED CONTENT

### Supporting Information

The Supporting Information is available free of charge at <https://pubs.acs.org/doi/10.1021/acs.chemmater.4c02454>.

Details for DP-GEN and NEP hyperparameters; evolution of the *a/c* ratio and lattice parameters; validation of the NEP model; and discussions on force fields (PDF)

## AUTHOR INFORMATION

### Corresponding Author

Yizhou Zhu – Research Center for Industries of the Future and School of Engineering, Westlake University, Hangzhou, Zhejiang 310030, China; [orcid.org/0000-0002-5819-7657](https://orcid.org/0000-0002-5819-7657); Email: [zhuyizhou@westlake.edu.cn](mailto:zhuyizhou@westlake.edu.cn)

### Author

Zihan Yan – School of Materials Science and Engineering, Zhejiang University, Hangzhou, Zhejiang 310027, China;

Research Center for Industries of the Future and School of Engineering, Westlake University, Hangzhou, Zhejiang 310030, China; [orcid.org/0000-0002-8911-6549](https://orcid.org/0000-0002-8911-6549)

Complete contact information is available at:

<https://pubs.acs.org/10.1021/acs.chemmater.4c02454>

## Author Contributions

Y. Zhu conceived, designed, and guided the research; Z. Yan performed the simulations; Y. Zhu and Z. Yan wrote the paper.

## Notes

The authors declare no competing financial interest.

## ACKNOWLEDGMENTS

We acknowledge the support from the Research Center for Industries of the Future (RCIF) and the High-Performance Computing Center (HPC) at Westlake University.

## REFERENCES

- (1) Zheng, F.; Kotobuki, M.; Song, S.; Lai, M. O.; Lu, L. Review on solid electrolytes for all-solid-state lithium-ion batteries. *J. Power Sources* **2018**, *389*, 198–213.
- (2) Wolfenstine, J.; Rangasamy, E.; Allen, J. L.; Sakamoto, J. High conductivity of dense tetragonal  $\text{Li}_7\text{La}_3\text{Zr}_2\text{O}_{12}$ . *J. Power Sources* **2012**, *208*, 193–196.
- (3) Liu, Q.; Geng, Z.; Han, C.; Fu, Y.; Li, S.; He, Y.-b.; Kang, F.; Li, B. Challenges and perspectives of garnet solid electrolytes for all solid-state lithium batteries. *J. Power Sources* **2018**, *389*, 120–134.
- (4) Wang, C.; Fu, K.; Kammampata, S. P.; McOwen, D. W.; Samson, A. J.; Zhang, L.; Hitz, G. T.; Nolan, A. M.; Wachsmann, E. D.; Mo, Y.; et al. Garnet-Type Solid-State Electrolytes: Materials, Interfaces, and Batteries. *Chem. Rev.* **2020**, *120*, 4257–4300.
- (5) Thompson, T.; Yu, S.; Williams, L.; Schmidt, R. D.; Garcia-Mendez, R.; Wolfenstine, J.; Allen, J. L.; Kioupakis, E.; Siegel, D. J.; Sakamoto, J. Electrochemical window of the Li-ion solid electrolyte  $\text{Li}_7\text{La}_3\text{Zr}_2\text{O}_{12}$ . *ACS Energy Lett.* **2017**, *2*, 462–468.
- (6) Thangadurai, V.; Narayanan, S.; Pinzaru, D. Garnet-type solid-state fast Li ion conductors for Li batteries: critical review. *Chem. Soc. Rev.* **2014**, *43*, 4714–4727.
- (7) Han, F.; Zhu, Y.; He, X.; Mo, Y.; Wang, C. Electrochemical stability of  $\text{Li}_{10}\text{GeP}_2\text{S}_{12}$  and  $\text{Li}_7\text{La}_3\text{Zr}_2\text{O}_{12}$  solid electrolytes. *Adv. Energy Mater.* **2016**, *6*, 1501590.
- (8) Chen, R.; Li, Q.; Yu, X.; Chen, L.; Li, H. Approaching practically accessible solid-state batteries: stability issues related to solid electrolytes and interfaces. *Chem. Rev.* **2020**, *120*, 6820–6877.
- (9) Wang, Y.; Lai, W. Phase transition in lithium garnet oxide ionic conductors  $\text{Li}_7\text{La}_3\text{Zr}_2\text{O}_{12}$ : The role of Ta substitution and  $\text{H}_2\text{O}/\text{CO}_2$  exposure. *J. Power Sources* **2015**, *275*, 612–620.
- (10) Chen, Y.; Rangasamy, E.; dela Cruz, C. R.; Liang, C.; An, K. A study of suppressed formation of low-conductivity phases in doped  $\text{Li}_7\text{La}_3\text{Zr}_2\text{O}_{12}$  garnets by in situ neutron diffraction. *J. Mater. Chem. A* **2015**, *3*, 22868–22876.
- (11) Bernstein, N.; Johannes, M.; Hoang, K. Origin of the structural phase transition in  $\text{Li}_7\text{La}_3\text{Zr}_2\text{O}_{12}$ . *Phys. Rev. Lett.* **2012**, *109*, 205702.
- (12) Geiger, C. A.; Alekseev, E.; Lazic, B.; Fisch, M.; Armbruster, T.; Langner, R.; Fechtelkord, M.; Kim, N.; Pettke, T.; Weppner, W. Crystal chemistry and stability of “ $\text{Li}_7\text{La}_3\text{Zr}_2\text{O}_{12}$ ” garnet: a fast lithium-ion conductor. *Inorg. Chem.* **2011**, *50*, 1089–1097.
- (13) Xu, M.; Park, M. S.; Lee, J. M.; Kim, T. Y.; Park, Y. S.; Ma, E. Mechanisms of  $\text{Li}^+$  transport in garnet-type cubic  $\text{Li}_{3+x}\text{La}_3\text{M}_2\text{O}_{12}$  ( $\text{M} = \text{Te}, \text{Nb}, \text{Zr}$ ). *Phys. Rev. B: Condens. Matter Mater. Phys.* **2012**, *85*, 052301.
- (14) Jaleem, R.; Yamamoto, Y.; Shiiba, H.; Nakayama, M.; Munakata, H.; Kasuga, T.; Kanamura, K. Concerted migration mechanism in the Li ion dynamics of garnet-type  $\text{Li}_7\text{La}_3\text{Zr}_2\text{O}_{12}$ . *Chem. Mater.* **2013**, *25*, 425–430.
- (15) Feng, Y.; Yang, L.; Yan, Z.; Zuo, D.; Zhu, Z.; Zeng, L.; Zhu, Y.; Wan, J. Discovery of high entropy garnet solid-state electrolytes via ultrafast synthesis. *Energy Storage Mater.* **2023**, *63*, 103053.
- (16) Klenk, M.; Lai, W. Local structure and dynamics of lithium garnet ionic conductors: tetragonal and cubic  $\text{Li}_7\text{La}_3\text{Zr}_2\text{O}_7$ . *Phys. Chem. Chem. Phys.* **2015**, *17*, 8758–8768.
- (17) Klenk, M. J.; Lai, W. Finite-size effects on the molecular dynamics simulation of fast-ion conductors: A case study of lithium garnet oxide  $\text{Li}_7\text{La}_3\text{Zr}_2\text{O}_{12}$ . *Solid State Ionics* **2016**, *289*, 143–149.
- (18) Dai, J.; Jiang, Y.; Lai, W. Study of diffusion and conduction in lithium garnet oxides  $\text{Li}_x\text{La}_3\text{Zr}_{x-5}\text{Ta}_{7-x}\text{O}_{12}$  by machine learning interatomic potentials. *Phys. Chem. Chem. Phys.* **2022**, *24*, 15025–15033.
- (19) Wang, S.; Liu, Y.; Mo, Y. Frustration in Super-Ionic Conductors Unraveled by the Density of Atomistic States. *Angew. Chem., Int. Ed.* **2023**, *62*, No. e202215544.
- (20) Geng, J.; Yan, Z.; Zhu, Y. Elucidating Anisotropic Ionic Diffusion Mechanism in  $\text{Li}_3\text{YCl}_6$  with Molecular Dynamics Simulations. *ACS Appl. Energy Mater.* **2024**, *7*, 7019–7024.
- (21) Kubicek, M.; Wachter-Welzl, A.; Rettenwander, D.; Wagner, R.; Berendts, S.; Uecker, R.; Amthauer, G.; Hutter, H.; Fleig, J. Oxygen vacancies in fast lithium-ion conducting garnets. *Chem. Mater.* **2017**, *29*, 7189–7196.
- (22) Paoletta, A.; Zhu, W.; Berton, G.; Savoie, S.; Feng, Z.; Demers, H.; Garipey, V.; Girard, G.; Rivard, E.; Delaporte, N.; et al. others Discovering the influence of lithium loss on garnet  $\text{Li}_7\text{La}_3\text{Zr}_2\text{O}_{12}$  electrolyte phase stability. *ACS Appl. Energy Mater.* **2020**, *3*, 3415–3424.
- (23) Kresse, G.; Hafner, J. Ab initio molecular-dynamics simulation of the liquid-metal–amorphous-semiconductor transition in germanium. *Phys. Rev. B: Condens. Matter Mater. Phys.* **1994**, *49*, 14251–14269.
- (24) Kresse, G.; Furthmüller, J. Efficient iterative schemes for ab initio total-energy calculations using a plane-wave basis set. *Phys. Rev. B: Condens. Matter Mater. Phys.* **1996**, *54*, 11169–11186.
- (25) Hohenberg, P.; Kohn, W. Inhomogeneous electron gas. *Phys. Rev.* **1964**, *136*, B864–B871.
- (26) Kohn, W.; Sham, L. J. Self-consistent equations including exchange and correlation effects. *Phys. Rev.* **1965**, *140*, A1133–A1138.
- (27) Blöchl, P. E. Projector augmented-wave method. *Phys. Rev. B: Condens. Matter Mater. Phys.* **1994**, *50*, 17953–17979.
- (28) Perdew, J. P.; Burke, K.; Ernzerhof, M. Generalized gradient approximation made simple. *Phys. Rev. Lett.* **1996**, *77*, 3865–3868.
- (29) Perdew, J. P.; Ruzsinszky, A.; Csonka, G. I.; Vydrov, O. A.; Scuseria, G. E.; Constantin, L. A.; Zhou, X.; Burke, K. Restoring the density-gradient expansion for exchange in solids and surfaces. *Phys. Rev. Lett.* **2008**, *100*, 136406.
- (30) Ong, S. P.; Richards, W. D.; Jain, A.; Hautier, G.; Kocher, M.; Cholia, S.; Gunter, D.; Chevrier, V. L.; Persson, K. A.; Ceder, G. Python Materials Genomics (pymatgen): A robust, open-source python library for materials analysis. *Comput. Mater. Sci.* **2013**, *68*, 314–319.
- (31) Wang, V.; Xu, N.; Liu, J.-C.; Tang, G.; Geng, W.-T. VASPKIT: A user-friendly interface facilitating high-throughput computing and analysis using VASP code. *Comput. Phys. Commun.* **2021**, *267*, 108033.
- (32) Momma, K.; Izumi, F. VESTA 3 for three-dimensional visualization of crystal, volumetric and morphology data. *J. Appl. Crystallogr.* **2011**, *44*, 1272–1276.
- (33) Novikov, I. S.; Gubaev, K.; Podryabinkin, E. V.; Shapeev, A. V. The MLIP package: moment tensor potentials with MPI and active learning. *Mach. Learn.: Sci. Technol.* **2021**, *2*, 025002.
- (34) Shapeev, A. V. Moment tensor potentials: A class of systematically improvable interatomic potentials. *Multiscale Model. Simul.* **2016**, *14*, 1153–1173.
- (35) Wang, H.; Zhang, L.; Han, J.; Weinan, E. DeepPMD-kit: A deep learning package for many-body potential energy representation and molecular dynamics. *Comput. Phys. Commun.* **2018**, *228*, 178–184.

- (36) Zeng, J.; Zhang, D.; Lu, D.; Mo, P.; Li, Z.; Chen, Y.; Rynik, M.; Huang, L.; Li, Z.; Shi, S.; et al. DeePMD-kit v2: A software package for deep potential models. *J. Chem. Phys.* **2023**, *159*, 054801.
- (37) Zhang, Y.; Wang, H.; Chen, W.; Zeng, J.; Zhang, L.; Wang, H.; Weinan, E. DP-GEN: A concurrent learning platform for the generation of reliable deep learning based potential energy models. *Comput. Phys. Commun.* **2020**, *253*, 107206.
- (38) Fan, Z.; Zeng, Z.; Zhang, C.; Wang, Y.; Song, K.; Dong, H.; Chen, Y.; Ala-Nissila, T. Neuroevolution machine learning potentials: Combining high accuracy and low cost in atomistic simulations and application to heat transport. *Phys. Rev. B* **2021**, *104*, 104309.
- (39) Fan, Z. Improving the accuracy of the neuroevolution machine learning potential for multi-component systems. *J. Phys.: Condens. Matter* **2022**, *34*, 125902.
- (40) Fan, Z.; Wang, Y.; Ying, P.; Song, K.; Wang, J.; Wang, Y.; Zeng, Z.; Xu, K.; Lindgren, E.; Rahm, J. M.; et al. GPUMD: A package for constructing accurate machine-learned potentials and performing highly efficient atomistic simulations. *J. Chem. Phys.* **2022**, *157*, 114801.
- (41) Song, K.; Zhao, R.; Liu, J.; Wang, Y.; Lindgren, E.; Wang, Y.; Chen, S.; Xu, K.; Liang, T.; Ying, P. General-purpose machine-learned potential for 16 elemental metals and their alloys. **2023**, arXiv:2311.04732. arXiv preprint.
- (42) Zhang, L.; Han, J.; Wang, H.; Car, R.; E, W. Deep potential molecular dynamics: a scalable model with the accuracy of quantum mechanics. *Phys. Rev. Lett.* **2018**, *120*, 143001.
- (43) He, X.; Zhu, Y.; Epstein, A.; Mo, Y. Statistical variances of diffusional properties from ab initio molecular dynamics simulations. *npj Comput. Mater.* **2018**, *4*, 18.
- (44) Kuganathan, N.; Rushton, M. J.; Grimes, R. W.; Kilner, J. A.; Gkanas, E. I.; Chroneos, A. Self-diffusion in garnet-type  $\text{Li}_7\text{La}_3\text{Zr}_2\text{O}_{12}$  solid electrolytes. *Sci. Rep.* **2021**, *11*, 451.
- (45) Li, Y.; Cao, Y.; Guo, X. Influence of lithium oxide additives on densification and ionic conductivity of garnet-type  $\text{Li}_{6.75}\text{La}_3\text{Zr}_{1.75}\text{Ta}_{0.25}\text{O}_{12}$  solid electrolytes. *Solid State Ionics* **2013**, *253*, 76–80.